Separation and Purification Technology 382 (2026) 135857

Contents lists available at ScienceDirect

Separation and Purification Technology

journal homepage: www.elsevier.com/locate/seppur

Experimental analysis of an upscaled reverse electrodialysis unit featuring electrode segmentation

Francesco Volpe, Emanuela Mangiaracina, Giuseppe Battaglia *, Andrea Cipollina, Giorgio Micale, Alessandro Tamburini

Università degli Studi di Palermo, Dipartimento di Ingegneria, Viale delle Scienze, 90128, Palermo, Italy

ARTICLE INFO

Editor: Gaohong He

Keywords:
Salinity gradient power
Green energy
Electrode segmentation
Reverse electrodialysis
Industrial scale set-up

ABSTRACT

Reverse electrodialysis (RED) is a technology that produces renewable energy from salinity gradients. In 2024, the EU has identified the RED process as a potential soon-to-be marketable technology for osmotic energy exploitation. For this purpose, high power densities and energy efficiencies are essential to achieve to increase the technology readiness level (TRL) of this technology. In this context, it is crucial to study the transition from lab-scale set-ups to pilot-scale units with larger membrane area. In this work, an upscaled RED unit (10 × 80 cm^2), equipped with segmented electrodes, was employed in an extensive experimental study where (i) flow velocities, (ii) high saline solution concentrations (up to 5.0 mol/L NaCl), and (iii) electrode configurations were varied to assess the influence of channels length on power generation and energy efficiency. Larger energy efficiencies obtained with long channels improved the overall power output and resources exploitation, reaching yield values of ~0.5 kWh/m^3, the highest ever reported in the literature. The electrode segmentation feature, explored for the first time with hypersaline solutions, allowed current density to be optimized across different sections of the unit, yielding up to a 21% increase in power density (maximum net power density of 4.1 W/m^2) compared to undivided electrodes. Results marked useful indications for future RED commercial implementation.

1. Introduction

Current environmental challenges (e.g., excessive CO_2 emissions, dwindling resources, and water scarcity) demand a significant shift from traditional paradigms of conventional production systems to innovative, sustainability-oriented approaches [1,2].

In the context of energy generation, salinity gradient energy (SGE), commonly defined as the renewable energy obtained through the controlled mixing of two solutions with different salinities, is still a promising and unexploited green source. The potential cumulative power from the river water discharged in oceans has been estimated to be in the range of 1.4–2.6 TW [3,4], which is comparable to the world electricity consumption of ~3.35 TW [5]. Unlike other renewable energy sources, such as solar or hydroelectric, SGE technologies offer the advantage of being weather-independent, non-intermittent and uniformly worldwide distributed [6,7]. Reverse Electrodialysis (RED) is one of the most advanced processes to harvest SGE [8]. Recently, in 2024, the EU has highlighted the RED as a soon to be marketable technology for potential osmotic energy exploitation [9].

RED is a membrane-based process that employs Ion Exchange Membranes (IEMs) (i.e. anionic, AEMs, and cationic, CEMs) to perform a selective separation of ions from saline solutions.

AEMs and CEMs allow, ideally, only anions or cations to pass through them, respectively. This is ensured by the presence of charged functional groups (with a charge opposite to that of the ions allowed to pass) inside the polymeric matrix of membranes [10].

In a RED unit, *stack*, CEMs and AEMs are alternately layered and separated by polymeric spacers or by profiles integrated into the membranes surface (i.e. *profiled membranes*). Spacers define the channels where solutions flow and, in addition, serve as mixing promoters to reduce concentration polarization phenomena [11–13]. The repetitive unit of RED, *cell pair*, is composed of a CEM, a channel for dilute solution, an AEM, and a channel for concentrated solution. The pile of cell pairs is enclosed by two electrodes, where redox reactions ($Ox + e^- \Leftrightarrow Ox^-$) convert ionic fluxes into electric current. Fig. 1 shows a schematic representation of a RED unit.

Numerous studies have been evaluating electrical power generation

* Corresponding author.
E-mail address: giuseppe.battaglia03@unipa.it (G. Battaglia).

https://doi.org/10.1016/j.seppur.2025.135857
Received 15 September 2025; Received in revised form 21 October 2025; Accepted 26 October 2025
Available online 29 October 2025

Nomenclature

A	Active cell pair area (m^2)
C_H	High saline solution molar concentration (mol/L)
C_L	Low saline solution molar concentration (mol/L)
C_M	Average saline solution molar concentration (mol/L)
E_{stack}	Stack voltage (V)
I	Electric current (A)
N	Number of cell pairs (−)
OCV	Open circuit voltage (V)
OCV_{Nernst}	Theoretical open circuit voltage (V)
P	Power (W)
P_d	Power density (W/m^2 cell pair)
$P_{d,gross}$	Gross power density (W/m^2 cell pair)
$P_{d,net}$	Net power density (W/m^2 cell pair)
P_{hydro}	Hydraulic power loss (W)
P_{stack}	Stack power (W)
Q	Volumetric flow rate (m^3/s)
Q_H	Volumetric flow rate of high saline solution (m^3/s)
Q_L	Volumetric flow rate of low saline solution (m^3/s)
R_{blank}	Blank resistance (Ω)
R_{load}	External load resistance (Ω)
R_{stack}	Stack resistance (Ω)
T	Temperature (K)
X	Exergy flow (W)
Y	Yield (kWh/m^3)
z	Valence number (−)

Greek

α_{AEM}	Permselectivity of anion exchange membrane (−)
α_{CEM}	Permselectivity of cation exchange membrane (−)
Δp	Pressure losses (Pa)
Δp_H	Pressure losses in high saline solution compartment (Pa)
Δp_L	Pressure losses in low saline solution compartment (Pa)
γ_H	High saline solution activity coefficient (−)
γ_L	Low saline solution activity coefficient (−)
η	Energy efficiency (%)
η_{gross}	Gross energy efficiency (%)
η_{net}	Net energy efficiency (%)

Abbreviations

AEM	Anion exchange membrane
CEM	Cation exchange membrane
ERS	Electrode rinse solution
IEM	Ion exchange membrane
OCV	Open circuit voltage
RED	Reverse electrodialysis
SGE	Salinity gradient energy

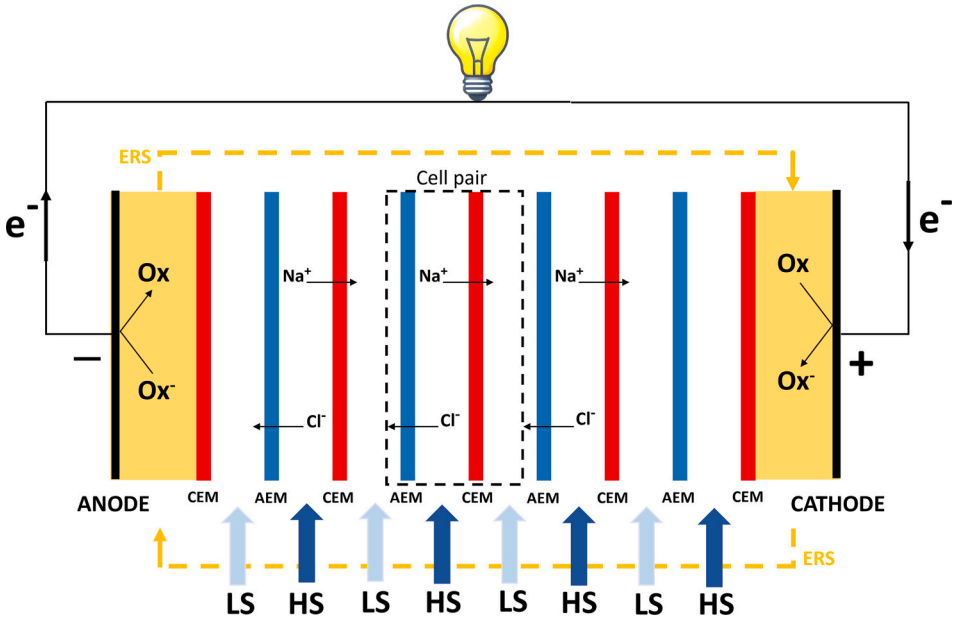

Fig. 1. RED Scheme. The dashed box indicates the Cell pair composed of one AEM, one CEM, high saline solution (HS) and low saline solution (LS) compartment. Electrode rinse solution (ERS) circulating in electrode compartments. (For interpretation of the references to colour in this figure legend, the reader is referred to the web version of this article.)

by RED units fed with river water and seawater saline solutions [14–17]. On the other hand, also more concentrated solutions have been investigated (saline concentration up to 300 g/L), such as brines from saltworks or desalination plants or highly concentrated industrial effluents [18,19]. The use of concentrated solutions allowed higher power densities to be achieved and, at the same time, constituted an environmentally friendly management of the concentrated solutions (dilution before discharge) [20,21]. Similarly, reclaimed wastewater has also been explored as possible diluted feed [22–25]. The performance of a RED unit is influenced by both macroscopic operating conditions and microscopic phenomena occurring near the membrane interfaces, where interfacial forces become significant [26–28].

Recently, several publications, both experimental and modelling, have focused on the development of innovative membranes, adopting emerging materials and investigating the nanoscale [29–31].

In the majority of published studies on RED, employed stacks are generally characterized by a limited active membrane area, typically around 10 × 10 cm^2 or 20 × 20 cm^2 [15,32–36]. However, for RED technology to be fully implemented at a commercial scale, it is essential to thoroughly assess the performance and challenges associated with stacks featuring large membrane areas or extended flow channels [37]. Indeed, while small membrane areas can achieve high power densities,

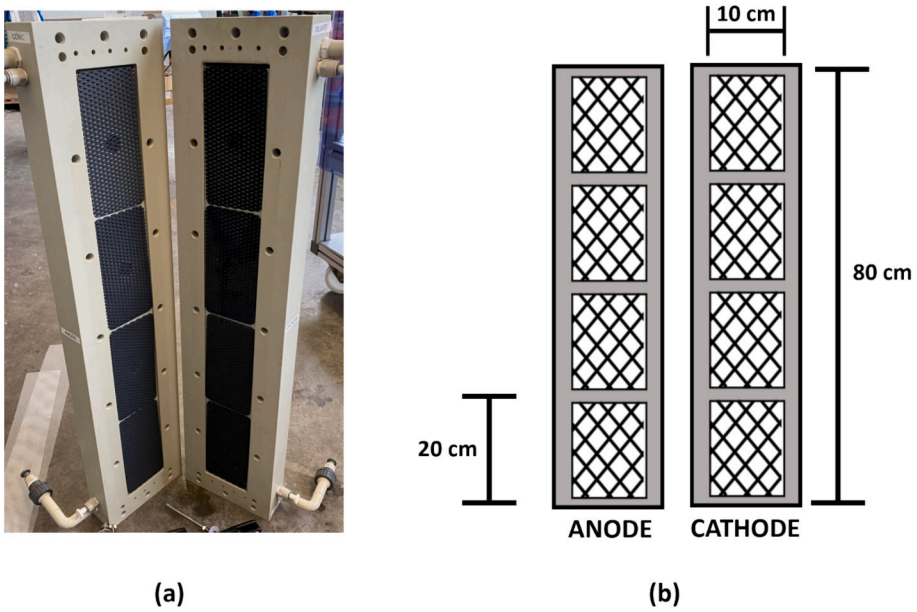

Fig. 2. (a) Picture of the RED unit (Electrodialysis module type 800, Deukum GmbH, Germany) equipped with segmented electrodes. (b) Schematic drawing of segmented electrodes structure. (For interpretation of the references to colour in this figure legend, the reader is referred to the web version of this article.)

stacks with larger membrane surfaces can yield higher energy efficiencies, enhancing total power output and reducing operational costs [38,39].

Among the several strategies aiming at optimizing the RED process, an innovative one is the use of stacks equipped with segmented electrodes. A segmented electrode is composed of multiple physically separated segments. This feature enables the connection of multiple electrical loads to a single RED stack, allowing current densities to be tuned locally across different regions of the membrane area. As the solutions flow along the channel length, their concentrations progressively change due to salt passage, resulting in varying internal resistance and electromotive force across different sections of the stack [38,40]. Electrode segmentation therefore allows for performance optimization by applying appropriately matched external loads to each electrode segment. Concentration changes intensify with increasing feed waters salinity gradient, due to more pronounced salt fluxes. Thereby, electrode segmentation may exert a stronger influence when hypersaline solutions are employed, since stack resistance exhibits greater variations.

Electrode segmentation is a relatively recent and still underexplored innovation. A first study on electrode segmentation in RED units was published by Veerman et al. [39] in 2010. The authors tested a 25 × 75 cm^2 RED pilot scale unit equipped with segmented electrodes divided into three 25 × 25 cm^2 pairs using artificial seawater and river water solutions. Power density increased of about 11%, from 0.44 W/m^2 to 0.49 W/m^2, when adopting the segmented configuration with respect to the case of "undivided parallel electrode". Since this study, only a limited number of works have been published. Pintossi et al. [38] investigated the performance of a 22 × 22 cm^2 cross-flow RED unit with electrode surface divided into four portions of 10 × 10 cm^2. The configuration with segmented electrodes led to an improvement in power density of 10%.

Veermas et al. [41] developed a numerical tool to evaluate the performance of a RED unit with segmented electrodes. The authors analysed a 10 × 10 cm^2 stack fed with seawater and river water. An increase in power density of 17% was obtained by subdividing the electrodes in 5 segments, although an increase of 13% was already predicted by adopting only 2 segments. The same author carried out an extensive modelling study to investigate the impact of electrode segmentation, feed flow configuration, and the seawater-to-river water ratio on the energy efficiency of a RED unit [34]. Results consistently demonstrated an improvement in energy efficiency when segmented electrodes were used. Across all tested seawater-to-river water ratios, the use of two electrode segments led to an average increase in energy efficiency of approximately 15% compared to the configuration with a single electrode. However, previous studies addressed the effect of segmented electrodes on RED process solely with seawater and river water solutions.

In the present work, the performance of an upscaled RED unit characterized by an industrial channel length of 80 cm was thoroughly investigated. The adopted unit was furnished with segmented electrodes, which allowed to characterize the stack with undivided electrode or multiple electrode segments. The goal of this study was to maximize energy generation from a given resource by identifying optimal strategies and operating conditions. A RED unit equipped with segmented electrodes was tested for the first time using synthetic hypersaline solutions exceeding seawater concentration. An extensive experimental campaign was conducted to assess the effect of long channels on RED performance, testing (i) flow velocities from 0.5 to 2.0 cm/s, (ii) NaCl concentrations from 1.0 to 5.0 mol/L, and (iii) multiple electrode configurations.

The operating conditions were set in view of the integration of RED power production from salinity gradient generated within an integrated treatment chain for the valorization of bitterns within the European project SEArcularMINE. With this respect, the RED unit operated after the quantitative recovery of magnesium and calcium from hypersaline solutions of Mediterranean sea saltworks, thus enabling to explore the full potential of RED, minimizing the detrimental influence of bivalent cations in the feed solutions, well known from literature studies.

2. Materials and methods

2.1. Experimental set-up

A 10 × 80 cm^2 industrial scale RED unit (Electrodialysis module type 800, Deukum GmbH, Germany), equipped with segmented electrodes, *DSA*, was adopted in the experimental campaign. A picture of the stack is shown in Fig. 2.a. Each electrode was composed of four segments with an active area of 10 × 20 cm^2 each, see Fig. 2.b. All electrode segments were rinsed by the same Electrode Rinse Solution (ERS), flowing in a single hydraulic circuit.

Table 1
Membrane types and characteristics. [42,43].

Membrane	Membrane Thickness (m 10^{-6})	Areal Resistance (Ω m^2 10^4)	Water Permeability (mL/(bar h m^2))	Permselectivity (%) (0.1–0.5 (mol/L) NaCl)	Burst strength [MPa]
AEM	125	1.7	6.5	94.5	2.75
CEM	135	2.0	6.5	94.7	2.75

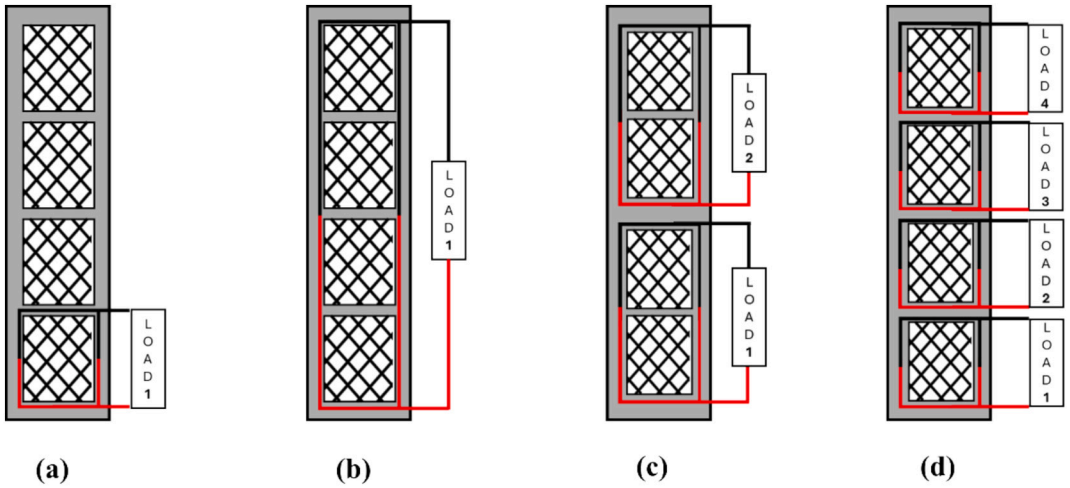

Fig. 3. Electrode configurations: (a) Configuration 1, (b) Configuration 2, (c) Configuration 3 and (d) Configuration 4.

Table 2
Operating conditions investigated in the present experimental campaign.

Operating conditions	Values
Flow velocity	0.5–1.0-2.0 cm/s
High saline solution concentration (C_H)	1.0–2.5-5.0 mol/L
Low saline solution concentration (C_L)	0.017 mol/L
Electrode configuration	Configuration 1 (10 × 20 cm^2 – one external load) Configuration 2 (10 × 80 cm^2 – one external load) Configuration 3 (10 × 80 cm^2 – two external loads) Configuration 4 (10 × 80 cm^2 – four external loads)

The stack was assembled with 10 cell pairs composed of (i) Fujifilm type 10 CEMs and AEMs, whose properties are reported in Table 1, and (ii) 270 μm thick woven spacers (Deukum GmbH, Germany) made of silicone and Polyethersulfone (PES). Fujifilm type 10 CEMs were also adopted as end-membranes. In each test, the solutions were fed in a co-current flow configuration, moving upward from the bottom, in an open-loop configuration. High and low saline solutions were made from deionized water and NaCl (99.5% purity, Saline di Volterra s.r.l., Italy) solutions, while for the ERS, a solution of 0.1 mol/L $K_4Fe(CN)_6 \bullet 3H_2O$ (99% purity ChemSolute®, Germany), 0.1 mol/L $K_3Fe(CN)_6$ (99% purity ChemSolute®, Germany) and 0.5 mol/L NaCl (99.5% purity, Saline di Volterra s.r.l., Italy) was used. The ERS solution was recirculated at a flow rate of 150 mL/min and stored in an opaque bottle. Three volumetric pumps (Lead Fluid YT15, peristaltic pump) were used for the hydraulic circuits: one for the ERS, one for the high and one for the low saline solution.

Pressure losses were measured through pressure gauges (Cewal S.p.a., Italy). Solution conductivity was monitored via a conductivity meter (WTW pH/Cond 3320). Multimeters (Fluke-175 True RMS, Everett, WA, USA) recorded the electric current and voltage. Resistance decade boxes were adopted to tune the external loads connected to the RED unit.

2.2. Electrode configurations

Four electrode configurations, see Fig. 3, were investigated: (i) Configuration 1, with only the first electrode segments pair (from the bottom of the stack) connected to an external load; (ii) Configuration 2, with all four electrode segments pairs connected to a single external load; (iii) Configuration 3, with the first two electrode segments pairs connected to a load and the other two to another one; and (iv) Configuration 4, with the four electrode segments pairs connected to four different external loads.

The comparison between Configurations 1 and 2 is proposed to investigate the influence of the channel length, namely 20 cm against 80 cm, on the performance of the RED system. For the sake of clarity, Configuration 1 corresponds to “partial area use configuration”, which was adopted in this work as a benchmark equivalent to a small-scale RED unit with a channel of 20 cm. From a practical perspective, this configuration is unlikely to be used in RED application, as it exploits only 25% of the total membrane area; accordingly, the results should be regarded as theoretical values. Consistent with the objectives of this study, power densities for Configuration 1 were calculated for an active membrane area of 10 × 20 cm^2, rather than the full membrane area.

The comparison between Configurations 2, 3 and 4 allows to assess the influence of the electrode segmentation feature at a fixed membrane area.

The electric current is determined by three factors: (i) electromotive force, (ii) internal resistance, and (iii) external loads. The first two parameters, in turn, depend on solution concentrations and therefore change along the channel length. Without electrode segmentation, only a single external load can be connected to the unit, whose value represents a compromise among the optimal conditions of the different sections of the total membrane area. This may induce dead zones, locations characterized by a low current and a limited power generation, and non-uniform current density distributions within the stack [38]. Electrode segmentation allows multiple external loads to be connected, thereby accounting for the variation in stack resistance and mitigating the

undesirable phenomena to optimize power density.

2.3. Experimental test design

Several operating conditions were investigated in a wide experimental campaign. Flow velocity, high saline solution concentration and electrode configuration were varied for a 3-factor full-factorial study. All experiments were carried out in triplicate to guarantee statistical reliability. The values included in the study are reported in Table 2.

The use of highly concentrated solutions may lead to performance losses due to a reduction of membrane permselectivity, as well as the risk of long-term issues such as scaling phenomena and deterioration in membrane properties. In this analysis, the influence of permselectivity decline with increasing concentrations was assessed as shown in the results section, whereas the investigation of long-term effects is left for future work involving extended operation test. However, Tedesco et al. reported that long term stability can be guaranteed when using hypersaline solutions [44], while a subsequent work of the same research group identified a performance decline in long term experiments adopting low saline solution which expose the membrane to the risks of carbonates scaling and biofouling [45]. Other published works [16,20,46–48] reported that, in long term tests, high saline compartments usually show lower fouling propensity than low salinity compartments. Evidence of scaling phenomena has been observed in [20,45] employing concentrated solutions up to 200 g/L. It is worth emphasizing that scaling phenomena in concentrated channels were mainly due to bivalent ions dissolved in solutions, such as Ca^{2+} and Mg^{2+}, which precipitate as carbonates. These species were not present in the synthetic solutions adopted in this work.

2.4. RED governing equations and definition of performance parameters

In a RED unit the maximum electromotive force for selected high and low saline solutions, *OCV*.

(Open Circuit Voltage), is achieved when no external load is connected to the stack. The theoretical open circuit voltage, OCV_{Nernst}, can be estimated from the Nernst equation:

$$OCV_{Nernst} = (\alpha_{CEM} + \alpha_{AEM})\frac{N \bullet R \bullet T}{z \bullet F} ln\left(\frac{\gamma_H C_H}{\gamma_L C_L}\right) \quad (1)$$

where α is the permselectivity of CEM and AEM (−), R is the universal gas constant (8.314 J/K•mol), N the number of cell pairs, T is the absolute temperature (K), z is the valence number (−), F is the Faraday constant (96,485C/mol) and γ is the activity coefficients (−) of high (γ_H) and low (γ_L) saline solutions. γ values were calculated following Pitzer's virial equation for a 1:1 electrolyte, as in the case of NaCl, see Section 2.1 in Supporting Information.

OCV_{Nernst} considers the inlet concentration values of solutions, so it does not account for non-Ohmic voltage drops such as concentration polarization phenomena and concentration gradient attenuation along the channel length [49]. Consequentially, the OCV value is always lower than OCV_{Nernst}.

When an external load is connected to the electrode connections of the RED unit, the electric current, I (A), flows across the external circuit and the potential difference measured at the electrodes, E_{Stack} (V), reduces due to internal stack resistance (Ω), R_{Stack}, as indicated by Eq. (2):

$$E_{stack} = OCV - R_{stack}I \quad (2)$$

The gross electric power density generated by a RED unit (W/m^2), $P_{d,stack}$, is calculated as:

$$P_{d,stack} = \frac{E_{stack}I}{N \bullet A} \quad (3)$$

where A is the active membrane area of a cell pair (m^2).

For ideal cases and perfect Ohmic behaviours, $P_{d,stack}$ follows a parabolic trend with the external voltage, reaching a maximum when E_{stack} is equal to $OCV/2$, i.e. where the external load resistance matches the value of R_{stack}.

The power output depends not only on the properties of membranes and solutions and on the operating conditions but also on the resistance of the electrode compartments (Ω), R_{blank}. The resistance and the consequent voltage drop at the electrode compartments are negligible in large units made of hundreds of cell pairs, while they have an impact on RED units assembled with a small number of cell pairs. In order to meaningfully compare the performance of a unit with a limited number of cell pairs to that of stack where the influence of R_{blank} is negligible, power density is typically "corrected" and the actual gross power density (W/m^2), $P_{d,gross}$, is calculated as [50–53]:

$$P_{d,gross} = \frac{OCV^2}{N \bullet A \bullet R_{load}\left(1 + \frac{R_{stack} - R_{blank}}{R_{load}}\right)} \quad (4)$$

where R_{load} is the resistance of the external load (Ω). R_{stack} and R_{blank} can be experimentally measured following procedure reported in the literature [18]. In Eq. (4) R_{blank} is subtracted to R_{stack} to isolate the resistance of membranes and saline solutions channels. The R_{blank} values used in Eq. (4) for each specific electrode configuration were derived from the areal blank resistance (Ω•m^2) measured in a 10 × 10 cm^2 stack employing the same membranes and ERS as in this study. This approach is well known and accepted for scale-up analysis with reliable results [50].

In the stack, the pumping losses (W), P_{hydro}, due to solution handling can be calculated as:

$$P_{hydro} = \Delta p_H Q_H + \Delta p_L Q_L \quad (5)$$

where Δp_H and Δp_L are the measured pressure losses between the inlet and outlet of high and low saline compartments (Pa), while Q_H and Q_L are the solutions flow rates (m^3/s). The pumping losses associated with the ERS compartments are typically excluded from the overall pumping losses, as its contribution becomes negligible in a scaled-up perspective (hundreds or thousands of cell pairs). In this study, pressure losses across the ERS compartments were barely measurable (lower than the limit of detection of 0.05 bar), resulting in an estimated pumping power lower than ~0.05 W.

The net power density, $P_{d,net}$, can be then evaluated as:

$$P_{d,net} = P_{d,gross} - \frac{P_{hydro}}{N \bullet A} \quad (6)$$

Direct measurements of the pressure losses at the first electrode segment location were not feasible, so the pressure losses for Configuration 1 were assumed to be equal to one quarter of those measured between the inlet and outlet of the unit. Consistently, pumping losses were normalized with respect to the actual active membrane area of this first segment (i.e., one quarter of the total area).

It is clear that, this assumption leads to an overestimation of net power for Configuration 1, as the total pressure drop comprises also pressure losses in the manifold and hydraulic circuit, which are independent of the channel length. Worth noting that pressure losses in manifolds can be up to 80% of the total pressure losses in a stack [54]. In this regard, a sensitivity analysis on the effect of pressure losses on $P_{d,net}$ and other performance parameters is reported in Section 2.3 in Supporting Information. Such analysis highlights how the assumption can have negligible influence on the net power density when manifold-related pressure losses stay within 25% of the total, or, if larger, when a higher salinity gradient potential is considered (e.g. the cases at C_H = 5.0 mol/L) or a low flow velocity is applied (i.e. 0.5 cm/s).

The *exergy flow*, X (W), is the maximum theoretical power that could be harvested for a certain pair of high and low concentrations and flowrates of saline solutions and can be estimated from the Gibbs free energy of reversible mixing process [17]:

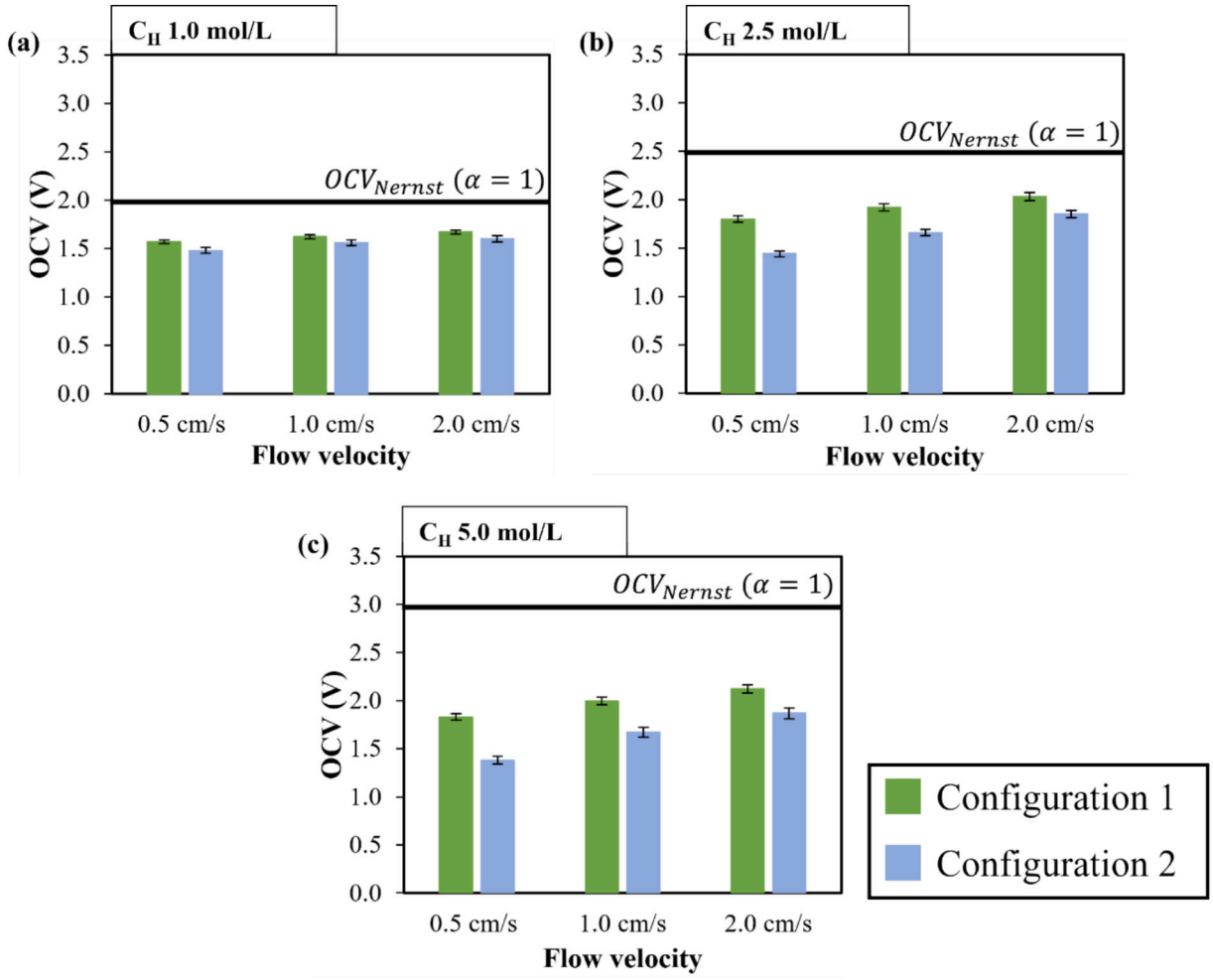

Fig. 4. OCV values measured in Configurations 1 and 2 adopting high saline solution concentrations of (a) 1.0 mol/L, (b) 2.5 mol/L and (c) 5.0 mol/L. High and low saline solutions flow velocities were 0.5, 1.0 and 2.0 cm/s. The low saline solution had a concentration of 0.017 mol/L in all tests. The black horizontal line is. OCV_{Nernst} calculated for ideal membrane (100% permselectivity).

$$X = 2RT\left[Q_H C_H ln\frac{\gamma_H C_H}{\gamma_{eq} C_{eq}} + Q_L C_L ln\frac{\gamma_L C_L}{\gamma_{eq} C_{eq}}\right] \quad (7)$$

where C_{eq} is the equilibrium concentration:

$$C_{eq} = \frac{C_H Q_H + C_L Q_L}{Q_H + Q_L} \quad (8)$$

The *energy efficiency*, η (%), of the RED unit can be the evaluated as the ratio between power output and exergy flow:

$$\eta = \frac{P_d \bullet N \bullet A}{X} \quad (9)$$

where P_d can be either the gross or the net power density.

The *yield* of the RED system, Y *(kWh/m^3),* can be defined as the amount of net power produced per cubic metre of feed solution:

$$Y = \frac{P_{d,net} \bullet N \bullet A}{Q} \quad (10)$$

where Q is the solutions flow rate.

3. Results

3.1. Single electrode configurations

In this section, the influence of channel length on *OCV* and power density values is assessed and discussed. Fig. 4 reports *OCV* values measured in Configurations 1 and 2 feeding high saline solutions at different concentrations, i.e. 1.0 mol/L, 2.5 mol/L and 5.0 mol/L, and different flow velocities, namely 0.5 cm/s, 1.0 cm/sand 2.0 cm/s. The low saline solution concentration was 0.017 mol/L in all tests.

At a fixed high saline solution concentration and flow velocity, OCV values were always, as expected, higher in tests conducted in Configuration 1 with respect to those of Configuration 2. This is due to a greater reduction in the concentration gradient along the channel length in Configuration 2, which resulted from its longer channel compared to Configuration 1. The attenuation in the concentration gradient was more pronounced at higher saline solution concentrations, whereas it diminished with increasing flow velocity.

These trends can be attributed to the typical dependence of the OCV on solution concentration and flow velocity [50]. Increasing the high saline solution concentration enhances the diffusive flux of ions from the high to the low saline solution channels, thereby reducing the driving force of the process. As concerns the velocity effect, higher flow velocities shorten the residence time, thereby limiting the reduction of the driving force. Apart from the test at high saline solution concentration of 5.0 mol/L and flow velocity of 0.5 cm/s, the discrepancies between OCV values in Configuration 1 and Configuration 2 were always lower than 20%.

A close inspection of Fig. 4 also reveals that, at a fixed high saline solution concentration, OCV values increased with flow velocity more in

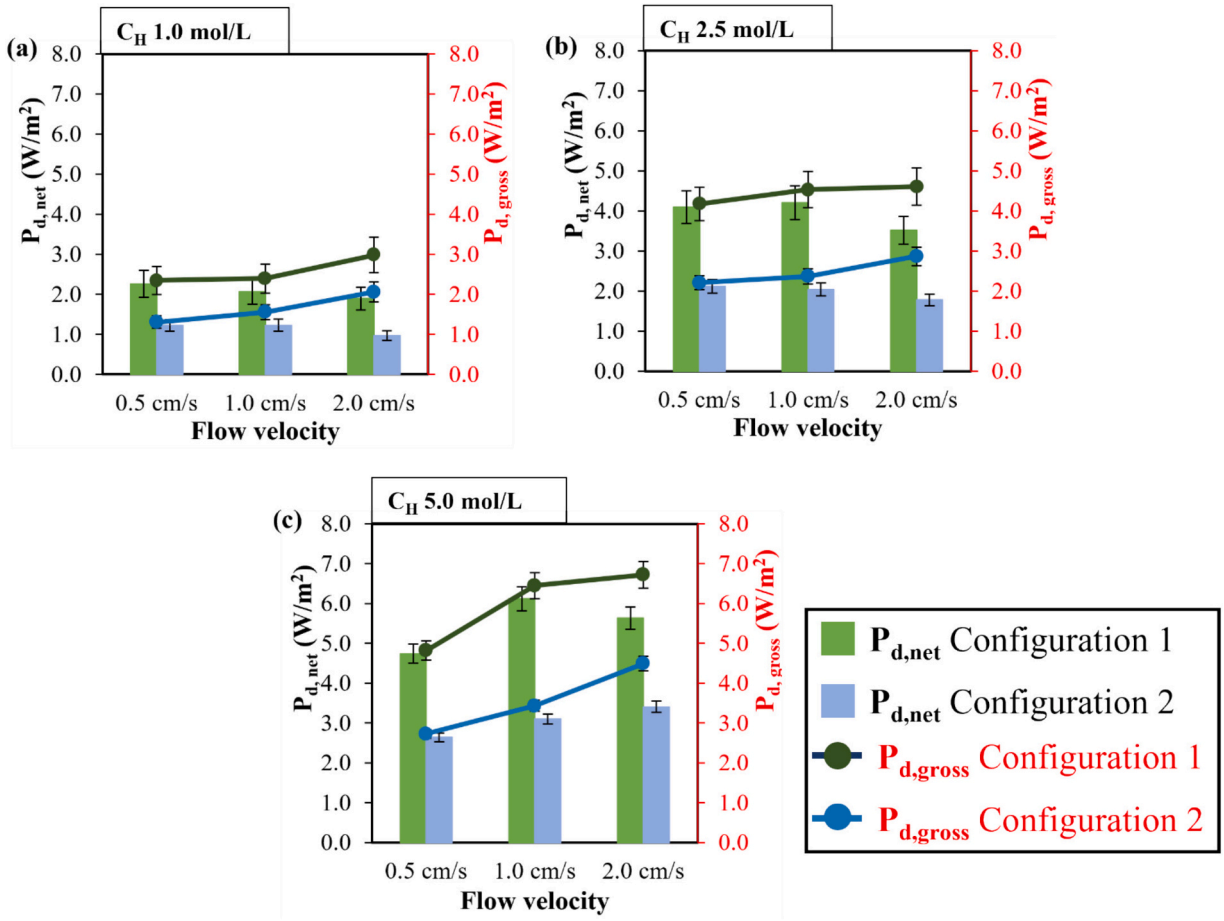

Fig. 5. Gross (lines with dots) and net (histograms) power density values for tests in Configurations 1 and 2 at high saline solution concentrations of (a) 1.0 mol/L, (b) 2.5 mol/L and (c) 5.0 mol/L. High and low saline solutions flow velocities were 0.5, 1.0 and 2.0 cm/s. The low saline solution had a concentration of 0.017 mol/L in all tests.

Configuration 1 than in Configuration 2. This is attributed to a more severe impact of salt passage between the solutions, which becomes more evident in longer channels at equal flow velocity (e.g. higher residence times). The better to highlight the influence of residence time on OCV, a comparison can be made between tests performed in Configuration 1 at a flow velocity of 0.5 cm/s and those in Configuration 2 at 2.0 cm/s (equal residence time of 40 s). At fixed high saline solution concentration, OCV values of Configuration 2 were equal or slightly higher than the values in Configuration 1. This behaviour, while confirming the influence of residence time on OCV values, may also be related to the enhancement of polarization coefficients with flow velocity, see Section 2.2 in Supporting Information, thus explaining the higher OCV values in Configuration 2 with respect to that of Configuration 1.

Regardless the adopted configuration, OCV values slightly increased from 1.0 mol/L to 2.5 mol/L, as high saline solution concentration, while values were almost the same using 2.5 mol/L and 5.0 mol/L solutions. The only exception was observed in Configuration 2 at a flow velocity of 0.5 cm/s, where an increase in concentration led to a detrimental effect on OCV values. As an example, considering Configuration 1 and flow velocity of 1.0 cm/s, OCV values were 1.7 V, 1.9 V and 2.0 V at high saline concentrations of 1.0 mol/L, 2.5 mol/L and 5.0 mol/L, respectively. The behaviour of OCV values can be attributed to the influence of saline solution concentration on the permselectivity of the membranes [15,55]. Avci et al. [39] reported that the permselectivity of various types of membranes decreased by approximately 20% when more concentrated NaCl solutions were used, specifically increasing from 0.1/0.5 mol/L to 0.5/4.0 mol/L. Similar results were also discussed by Daniilidis et al. [56] that observed a reduction in membranes permselectivity of ~20–30% using river water and different highly concentrated NaCl solutions. The influence of permselectivity is here emphasized from a comparison between measured OCV values and theoretical OCV_{Nernst} ones calculated for ideal membranes (100% permselectivity). As expected, the deviation from the ideal values was more pronounced at higher saline solution concentrations. Referring to tests performed in Configuration 1 at flow velocity of 2.0 cm/s (cases less affected by non-Ohmic voltage drops due to the highest adopted velocity and shortest channel), the estimated permselectivity (given by the ratio $OCV/OCV_{Nernst\ (\alpha=1)}$) would be ~0.95, ~0.83 and 0.73 for high saline solution concentration of 1.0 mol/L, 2.5 mol/L and 5.0 mol/L, respectively. Permselectivity values agree with those calculated using Eq. (A.7) reported in Giacalone et al. [57] for the same membranes, i.e. Fujifilm type 10, as supplied by the manufacturer. Specifically, values were 0.95, 0.87, 0.76 for high saline solution concentration of 1.0 mol/L, 2.5 mol/L and 5.0 mol/L, respectively.

Overall, regardless of electrode configuration, the best OCV values were observed at a high saline solution concentration of 5.0 mol/L and a flow velocity of 2.0 cm/s, reaching 2.1 V and 1.9 V for Configuration 1 and Configuration 2, respectively.

The impact of the industrial scale channel on RED performance, in comparison to the partial area use of Configuration 1, was further evaluated by analysing the gross and net power density values across all investigated cases, as reported in Fig. 5.

The highest net and gross power density values were observed in Configuration 1 due to a higher average salinity gradient.

Gross power density was observed to increase with flow velocity,

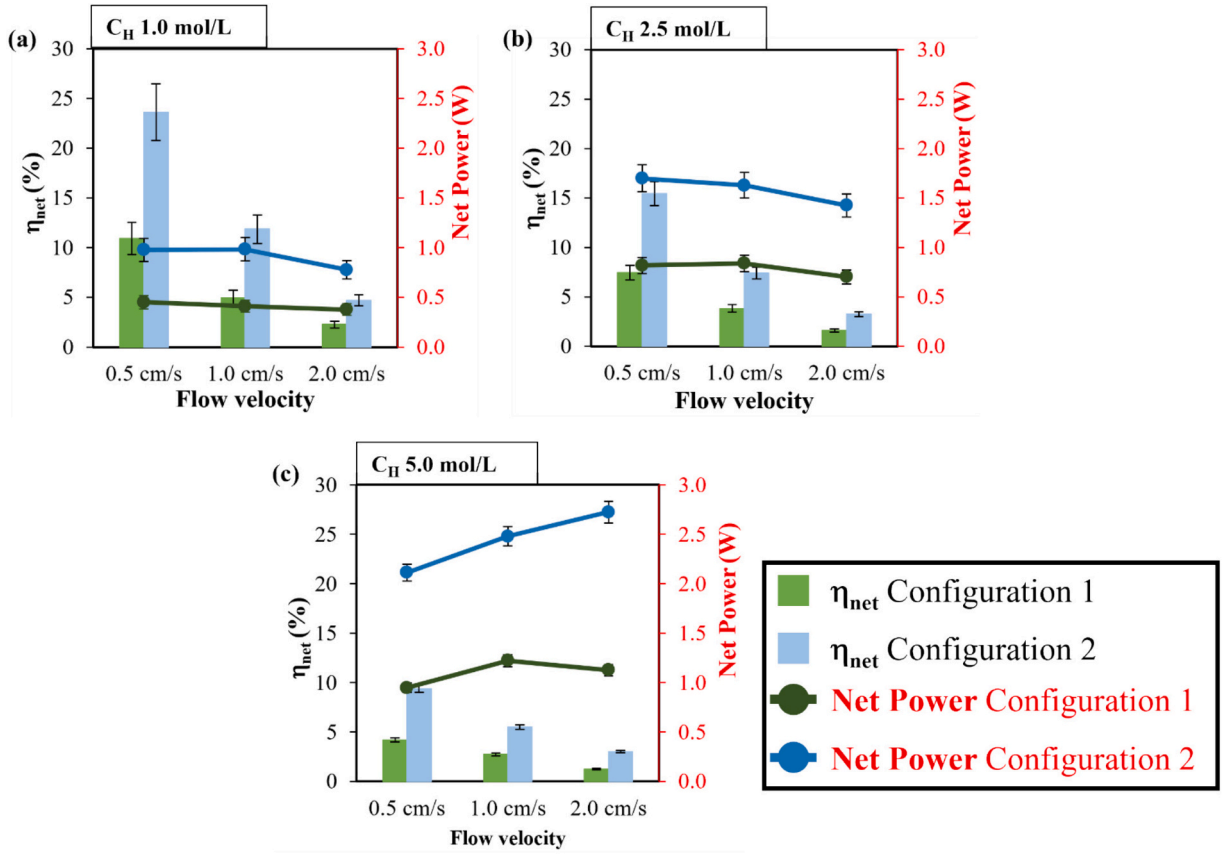

Fig. 6. Net Power (lines with dots) and energy efficiency (histograms) for tests in Configurations 1 and 2 at high saline solution concentrations of (a) 1.0 mol/L, (b) 2.5 mol/L and (c) 5.0 mol/L. High and low saline solutions flow velocities were 0.5, 1.0 and 2.0 cm/s in each case. The low saline solution had a concentration of 0.017 mol/L in all tests.

regardless the solution concentration and channel length. This is consistent with the results reported in literature [15]. In Configuration 1, the improvement of gross power density with flow velocity was less pronounced compared to Configuration 2 at high saline solution concentrations of 2.5 mol/L and 5.0 mol/L. This highlights the need for higher flow velocities in long stacks to mitigate salt passage between channels and preserve the salinity gradient. Nevertheless, net power density values exhibited a completely different trend, suggesting that different operating conditions should be considered as the optimal working point. In fact, from Fig. 5, it can be noticed that in all cases, with exception of test at $C_H = 5.0$ mol/L and Configuration 2, an increase of the velocity from 1.0 cm/s to 2.0 cm/s caused a reduction of the net power density. It should be emphasized that, regardless the configuration, the trend of power density values with increasing high saline solution concentration does not follow the corresponding trend of OCV values. Indeed, at fixed flow velocity, an appreciable enhancement in power density was recorded from 1.0 mol/L to 2.5 mol/L and a more marked increase was observed from 2.5 mol/L to 5.0 mol/L. As an example, considering Configuration 2 and a velocity of 1.0 cm/s, net power density values were 1.5 W/m^2, 2.2 W/m^2 and 3.0 W/m^2 at high saline concentrations of 1.0 mol/L, 2.5 mol/L and 5.0 mol/L, respectively.

In fact, despite the OCV trends, which in most cases exhibited small variations with increasing concentration, higher saline solution concentrations led to lower stack resistance and to a more pronounced salinity gradient along the channel length. Consequently, the measured stack currents increased with solution concentration, thus enhancing power density.

In Configuration 1 the highest value of net power density was recorded for the test performed at $C_H = 5.0$ mol/L and a flow velocity of 1.0 cm/s, being 6.1 W/m^2 (±0.3 W/m^2), while for Configuration 2 the highest value was still obtained for a high saline solution concentration of 5.0 mol/L but at a flow velocity of 2.0 cm/s, being 3.4 W/m^2 (±0.2 W/m^2).

Noteworthy, the power density values were also affected by perm-selectivity losses. According to Eq. (4), if ideal membranes were adopted, the gross power density would increase by ~10%, ~45% and ~90% for tests performed with high saline solution concentration of 1.0 mol/L, 2.5 mol/L and 5.0 mol/L, respectively. Under these considerations, the maximum theoretical value of net power density would be 11.7 W/m^2, for the high saline solution concentration of 5.0 mol/L at a flow velocity of 1.0 cm/s in Configuration 1. Theoretical net power densities are reported in Appendix A1.

Although higher values of power density were recorded with a partial area use, i.e. Configuration 1, the actual power output was instead higher in Configuration 2. This can be visualized referring to the net power and net energy efficiency in Fig. 6.

From Fig. 6, net power was notably higher in Configuration 2. In detail, the maximum net power value of 2.7 W was obtained at high saline solution concentration of 5.0 mol/L and a flow velocity of 2.0 cm/s. The improvement in net power values achieved in Configuration 2 strongly supports the use of industrial scale stacks for RED applications. Indeed, under fixed operating conditions, net power values in Configuration 2 were consistently at least twice higher than those obtained in Configuration 1. This analysis demonstrated that the extended channel length of the RED unit, compared to the typical lengths used in lab-scale set-ups (10–20 cm), was still able to harvest a not negligible amount of renewable energy, despite operating under a reduced salinity gradient. It should be also noted that the enhancement observed in this study was achieved while maintaining the same flow rate, thereby keeping

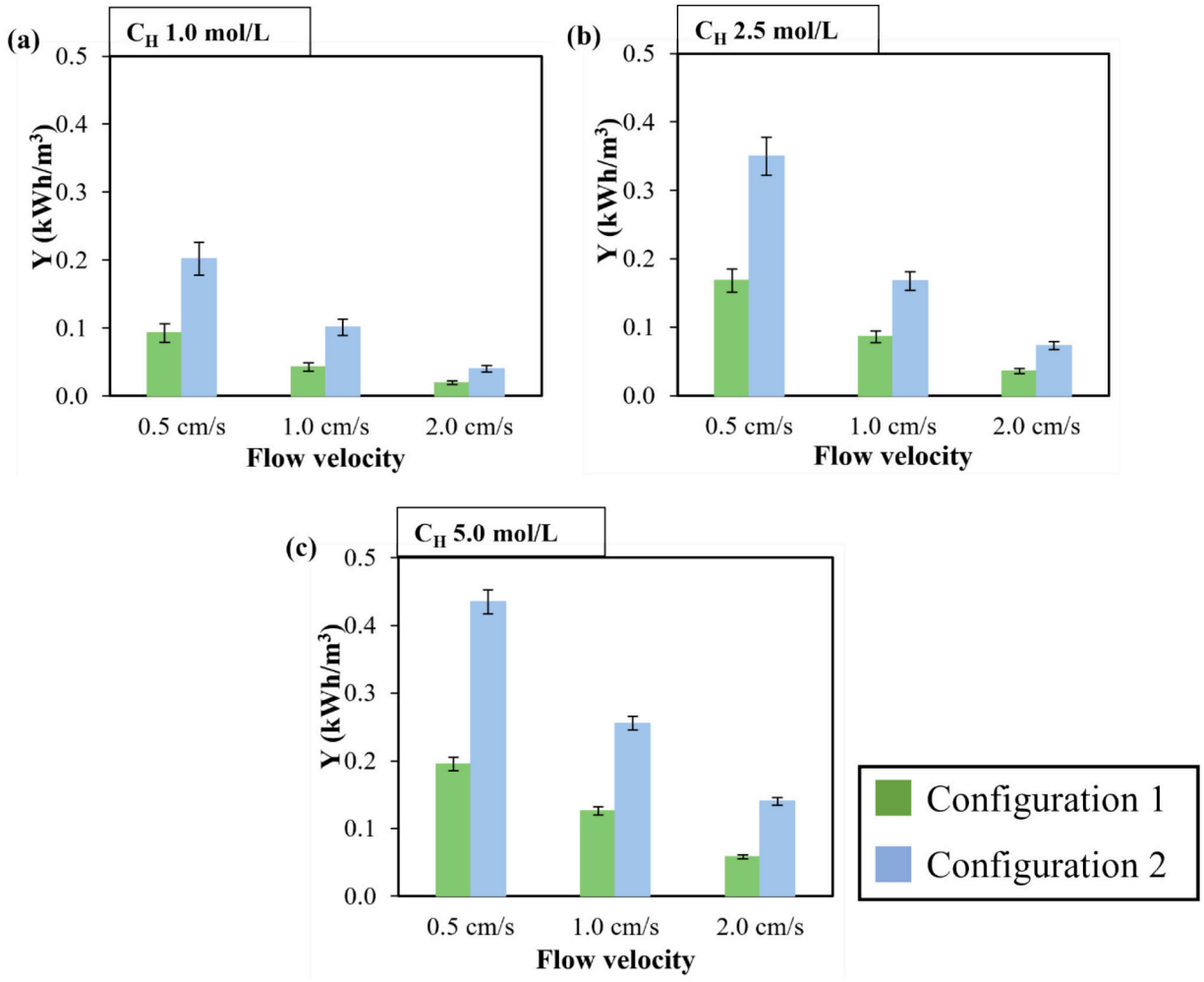

Fig. 7. Yield for tests in Configurations 1 and 2 at high saline solution concentrations of (a) 1.0 mol/L, (b) 2.5 mol/L and (c) 5.0 mol/L. High and low saline solutions flow velocities were 0.5, 1.0 and 2.0 cm/s in each case. The low saline solution had a concentration of 0.017 mol/L in all tests.

solution and resource consumption constant. In other words, it is not necessary to match the residence time by increasing the flow rate, with associated increasing operative costs. On the contrary, operating at the same residence time implies a higher solution consumption and even a reduction in performance compared to maintaining the same flow velocity, see Fig. 6.

The reduction in OCV values observed in Fig. 4, when moving from Configuration 1 to Configuration 2, at fixed flow velocity and concentration, was compensated by lower stack resistances and higher electric currents enabled by the larger membrane area. In particular, the effect of stack resistance reduction was prominent compared to the decrease in OCV, thus leading to an overall enhancement of the net power output (see Eq. (4)). OCV and resistance values measured during the tests are reported in Appendix A2.

Regarding net energy efficiency, values consistently decreased with increasing flow velocity and high saline solution concentration, as reported in other literature works [43], indicating that the rise in exergy flow consistently outweighed the improvement in net power density. Concerning comparison between configurations, net energy efficiency followed trends similar to those of net power; accordingly, the same considerations hold, with net energy efficiency values in Configuration 2 being more than twice those attained in Configuration 1 under fixed operating conditions. Overall, the best net energy efficiency value was observed in Configuration 2 at the lowest high saline solution concentration (1.0 mol/L) and the lowest flow velocity (0.5 cm/s), being 23.6% (±2.5%).

In the tests, the high saline solutions retained a concentration close to the initial one, as demonstrated by the analysis of solution samples taken from the outlet sections of the stack (see Section 2.5 in Supporting Information), thus indicating the use of either longer channels or a multistage pass of the high saline solution to improve energy exploitation, as also discussed in [58]. Moreover, despite additional auxiliary equipment needed and a more complex system, a multi-stage approach better accounts for variations in the salinity gradient, since membrane type, spacer geometry, number of cell pairs, and flow velocity can be adjusted in subsequent units to maximize power output. The exploited salinity gradient from solution can also be highlighted referring to yield, Y, as reported in Fig. 7.

At a fixed high saline solution concentration and configuration, yield values decreased with increasing flow velocity, as also reported in previous studies [7], indicating that lower velocities allow better energy harvesting from the same amount of feedwaters, see Fig. 7. Yield values increased with solution concentration, as a result of the enhanced power output. Specifically, the maximum yield of 0.44 kWh/m^3 (±0.02 kWh/m^3) was obtained in Configuration 2 at high saline solution concentration of 5.0 mol/L and a flow velocity of 0.5 cm/s, marking a significant improvement over previous results reported in literature for RED operation with comparable solutions [44]. Once again, the use of long channels was found to be a potential way to achieve higher performance with the same resource consumption.

A more detailed economic analysis, which is out of the scope of this work, would be required to effectively assess the optimal channel length

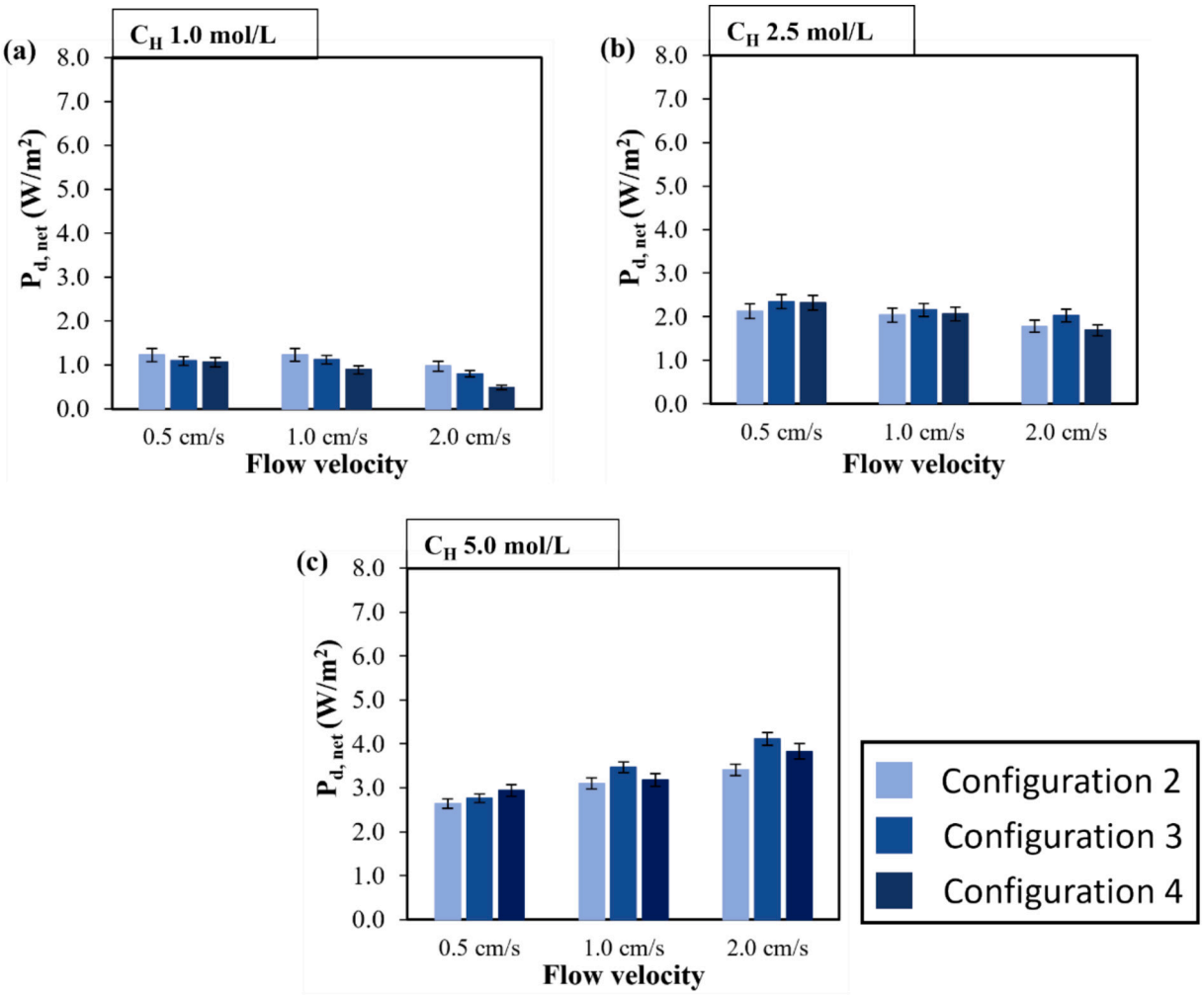

Fig. 8. Net power density for tests operated in Configurations 2, 3 and 4 at high saline solution concentrations of (a) 1.0 mol/L, (b) 2.5 mol/L and (c) 5.0 mol/L. High and low saline solutions flow velocities were 0.5, 1.0 and 2.0 cm/s in each case. The low saline solution had a concentration of 0.017 mol/L in all tests.

Table 3
Summary of works on RED systems equipped with electrode segmentation.

	References	Active membrane area (cm^2)	Number of segments	C_H (mol/L)	C_L (mol/L)	$P_{d,net}$ (W/m^2)*	Maximum power Density increase Due to segmentation
Veerman et al. 2010	[39]	25 × 75	3	0.017	0.5	1.0	11%
Pintossi et al. 2020	[38]	22 × 22	4	0.017	0.5	1.6	10%
This work	[–]	10 × 80	2	0.017	5.0	4.1	21%
This work	[–]	10 × 80	4	0.017	5.0	3.8	12%

* Net power densities are expressed referring to total cell pair area.

Table 4
Summary of upscaled RED units in literature.

	References	**Active membrane area (cm^2)**	**C_H (mol/L)**	**C_L (mol/L)**	**Flow velocity (cm/s)**	**$P_{d,net}$ (W/m^2)***
Veerman et al. 2010	[39]	25 × 75	0.017	0.5	1.0	1.0
Tedesco et al. 2016	[18]	44 × 44	0.03	4.0–5.0	1.0	1.6 real solutions 2.8 synthetic solutions
Tedesco et al. 2017	[3]	44 × 44	0.007–0.060	4.0	0.9	1.8 real solutions
Nam et al. 2019	[24]	29 × 43	0.01–0.06	0.5	1.5	0.8
This work	[–]	10 × 80	0.017	5.0	2.0	4.1

* Net power densities are expressed referring to total cell pair area.

Table A1
$P_{d,net}$ and theoretical $P_{d,net}$ in the experimental campaign.

C_H (mol/L)	Flow velocity (cm/s)	Configuration	$P_{d,net}$ (W/m^2)	Theoretical $P_{d,net}$ (W/m^2)
1.0	0.5	1	2.3	2.5
1.0	0.5	2	1.2	1.4
1.0	1.0	1	2.1	2.3
1.0	1.0	2	1.2	1.4
1.0	2.0	1	1.9	2.2
1.0	2.0	2	1.0	1.2
2.5	0.5	1	4.1	6.0
2.5	0.5	2	2.1	3.1
2.5	1.0	1	4.2	6.2
2.5	1.0	2	2.0	3.1
2.5	2.0	1	3.5	5.6
2.5	2.0	2	1.8	3.1
5.0	0.5	1	4.7	9.0
5.0	0.5	2	2.7	5.0
5.0	1.0	1	6.1	11.7
5.0	1.0	2	3.1	6.1
5.0	2.0	1	5.6	11.5
5.0	2.0	2	3.4	7.3

Table A2
Comparison of Configurations 1 and 2 in terms of OCV, stack resistance, net power.

C_H (mol/L)	Flow velocity (cm/s)	Configuration	OCV (V)	Stack resistance (Ω)	Net power (W)
1.0	0.5	1	1.57	1.44	0.45
1.0	0.5	2	1.48	0.46	0.98
1.0	1.0	1	1.62	1.49	0.42
1.0	1.0	2	1.56	0.48	0.98
1.0	2.0	1	1.67	1.54	0.38
1.0	2.0	2	1.6	0.49	0.78
2.5	0.5	1	1.88	1.18	0.82
2.5	0.5	2	1.4	0.35	1.70
2.5	1.0	1	1.92	1.24	0.84
2.5	1.0	2	1.66	0.37	1.63
2.5	2.0	1	2.03	1.35	0.70
2.5	2.0	2	1.85	0.37	1.42
5.0	0.5	1	1.83	0.89	0.95
5.0	0.5	2	1.38	0.27	2.11
5.0	1.0	1	2.00	1.01	1.22
5.0	1.0	2	1.67	0.28	2.48
5.0	2.0	1	2.12	1.13	1.13
5.0	2.0	2	1.87	0.29	2.73

and operating conditions. However, it should be noted that, in addition to the improvement in power output discussed here, RED units with longer channels can reduce the relative impact of material usage, operation costs or auxiliary equipment, such as (i) the membrane area inactive as it is covered by gaskets; (ii) pumping losses due to localized and manifold pressure drops; (iii) hydraulic circuits and instrumentation. Giacalone et al. [57] demonstrated that, although the optimal configuration is not always achieved with the longest channel, systems coupling fresh water and hypersaline brine units benefit from the use of long channels, even 1.0 m, achieving lower levelized cost of energy.

In conclusion, the improvements in resource utilization achieved in Configuration 2—highlighted in terms of net power, net energy efficiency, and yield—demonstrate that longer channels enable larger energy harvesting due to a better exploitation of the salinity gradient power potential, as also reported in some previous studies [37,39].

3.2. Segmented electrode configurations

The benefits of the use of multiple electric circuits in the industrial scale RED unit, exploiting the segmented electrodes, was investigated by employing hypersaline solutions (up to 5.0 mol/L NaCl). Fig. 8 shows the net power densities achieved in the tests performed in

Table B1
OCV values for tests performed in Configuration 2, 3 and 4.

Experimental test		Configuration 2	Configuration 3	Configuration 4
Flow velocity 0.5 cm/s C_H 1.0 mol/L C_L 0.017 mol/L	First segment OCV (V)	1.48	1.52	1.65
	Second segment OCV (V)			1.17
	Third segment OCV (V)		0.96	0.95
	Fourth segment OCV (V)			0.79
Flow velocity 1.0 cm/s C_H 1.0 mol/L C_L 0.017 mol/L	First segment OCV (V)	1.56	1.65	1.70
	Second segment OCV (V)			1.33
	Third segment OCV (V)		1.20	1.16
	Fourth segment OCV (V)			1.01
Flow velocity 2.0 cm/s C_H 1.0 mol/L C_L 0.017 mol/L	First segment OCV (V)	1.60	1.78	1.74
	Second segment OCV (V)			1.45
	Third segment OCV (V)		1.39	1.32
	Fourth segment OCV (V)			1.19
Flow velocity 0.5 cm/s C_H 2.5 mol/L C_L 0.017 mol/L	First segment OCV (V)	1.44	1.65	1.75
	Second segment OCV (V)			1.28
	Third segment OCV (V)		1.10	1.04
	Fourth segment OCV (V)			0.86
Flow velocity 1.0 cm/s C_H 2.5 mol/L C_L 0.017 mol/L	First segment OCV (V)	1.66	1.83	1.95
	Second segment OCV (V)			1.52
	Third segment OCV (V)		1.33	1.30
	Fourth segment OCV (V)			1.13
Flow velocity 2.0 cm/s C_H 2.5 mol/L C_L 0.017 mol/L	First segment OCV (V)	1.85	1.97	2.07
	Second segment OCV (V)			1.76
	Third segment OCV (V)		1.54	1.57
	Fourth segment OCV (V)			1.44

(continued on next page)

Table B1 (*continued*)

Experimental test		Configuration 2	Configuration 3	Configuration 4
Flow velocity 0.5 cm/s C_H 5.0 mol/L C_L 0.017 mol/L	First segment OCV (V)	1.38	1.66	1.90
	Second segment OCV (V)			1.30
	Third segment OCV (V)		1.08	1.00
	Fourth segment OCV (V)			0.83
Flow velocity 1.0 cm/s C_H 5.0 mol/L C_L 0.017 mol/L	First segment OCV (V)	1.67	1.84	2.01
	Second segment OCV (V)			1.54
	Third segment OCV (V)		1.37	1.29
	Fourth segment OCV (V)			1.13
Flow velocity 2.0 cm/s C_H 5.0 mol/L C_L 0.017 mol/L	First segment OCV (V)	1.87	2.02	2.14
	Second segment OCV (V)			1.75
	Third segment OCV (V)		1.61	1.52
	Fourth segment OCV (V)			1.39

Configurations 2, 3 and 4, using saline solutions concentrations of 1.0 mol/L, 2.5 mol/L and 5.0 mol/L, and different flow velocities, namely 0.5 cm/s, 1.0 cm/s and 2.0 cm/s. The low saline solution concentration was 0.017 mol/L in all tests.

For the tests conducted at a high saline solution concentration of 1.0 mol/L, see Fig. 8.a, the highest net power density values were obtained in Configuration 2. As the high saline solution concentration increased, the benefits of electrode segmentation became progressively more evident. At high saline solution concentration equal to 2.5 mol/L, Fig. 8.b, the net power density values for both Configurations 3 and 4 were higher or at least equal to those obtained with Configuration 2. Specifically, Configuration 3 consistently performed best across the three tests, showing an increase of ~10% compared to the case of undivided electrodes, from 2.1 to 2.3 W/m^2, at 0.5 cm/s, from 2.0 to 2.2 W/m^2, at 1.0 cm/s, and from 1.8 to 2.0 W/m^2, at 2.0 cm/s, respectively. Conversely, Configuration 4 exhibited similar results of Configuration 2, gaining a slight improvement of power density only at flow velocity of 0.5 cm/s, from 2.1 to 2.3 W/m^2. At high saline solution concentration of 5.0 mol/L, Fig. 8.c, the influence of segmented electrodes was more meaningful. Configuration 3 was again the best one at flow velocities of 1.0 cm/s and 2.0 cm/s, showing an improvement of at least of 10% and a maximum of 21% (±8%) at flow velocity of 2.0 cm/s, from 3.4 W/m^2 to 4.1 W/m^2. The latter power density value corresponds to a net power of 3.3 W.

Configuration 4 provided the highest value among configurations at flow velocity of 0.5 cm/s, with a power density increase of ~10% with respect to Configuration 2. In addition, a value of yield of 0.48 kWh/m^3 (±0.02 kWh/m^3) was obtained in the test at 0.5 cm/s in Configuration 4, being the highest value of the overall experimental campaign. Configuration 4 had similar results of those of Configuration 2 at flow velocity of 1.0 cm/s, while it overperformed them of about 10% at flow velocity of 2.0 cm/s. The maximum value of net power density recorded among

Table B2
Current density values for tests performed in Configurations 2, 3 and 4.

Experimental test		Configuration 2	Configuration 3	Configuration 4
Flow velocity 0.5 cm/s C_H 1.0 mol/L C_L 0.017 mol/L	First segment current density (A/m^2)	19.7	19.2	18.8
	Second segment current density (A/m^2)			21.1
	Third segment current density (A/m^2)		20.4	22.9
	Fourth segment current density (A/m^2)			17.6
Flow velocity 0.5 cm/s C_H 2.0 mol/L C_L 0.017 mol/L	First segment current density (A/m^2)	23.7	18.6	15.1
	Second segment current density (A/m^2)			23.0
	Third segment current density (A/m^2)		24.1	26.6
	Fourth segment current density (A/m^2)			21.6
Flow velocity 1.0 cm/s C_H 1.0 mol/L C_L 0.017 mol/L	First segment Current density (A/m^2)	30.5	21.8	20.4
	Second segment current density (A/m^2)			25.0
	Third segment current density (A/m^2)		25.5	28.5
	Fourth segment current density (A/m^2)			24.2
Flow velocity 0.5 cm/s C_H 2.5 mol/L C_L 0.017 mol/L	First segment current density (A/m^2)	25.3	31.4	30.8
	Second segment current density (A/m^2)			36.5
	Third segment current		30.6	41.8

(*continued on next page*)

Table B2 (*continued*)

Experimental test		Configuration 2	Configuration 3	Configuration 4
	density (A/m^2)			
	Fourth segment current density (A/m^2)			25.2
Flow velocity 1.0 cm/s C_H 2.5 mol/L C_L 0.017 mol/L	First segment Current density (A/m^2)	34.4	34.7	31.8
	Second segment current density (A/m^2)			39.1
	Third segment current density (A/m^2)		37.0	49.4
	Fourth segment current density (A/m^2)			35.6
Flow velocity 2.0 cm/s C_H 2.5 mol/L C_L 0.017 mol/L	First segment current density (A/m^2)	36.4	36.8	25.7
	Second segment current density (A/m^2)			37.9
	Third segment current density (A/m^2)		40.8	38.6
	Fourth segment current density (A/m^2)			41.7
Flow velocity 0.5 cm/s C_H 5.0 mol/L C_L 0.017 mol/L	First segment current density (A/m^2)	35.8	37.8	42.9
	Second segment current density (A/m^2)			57.1
	Third segment current density (A/m^2)		23.4	49.0
	Fourth segment current density (A/m^2)			54.4
Flow velocity 1.0 cm/s C_H 5.0 mol/L C_L 0.017mol/L	First segment current density (A/m^2)	42.0	41.4	36.3
	Second segment current			46.5

Table B2 (*continued*)

Experimental test		Configuration 2	Configuration 3	Configuration 4
	density (A/m^2)			
	Third segment current density (A/m^2)		39.5	51.7
	Fourth segment current density (A/m^2)			39.7
Flow velocity 2.0 cm/s C_H 5.0 mol/L C_L 0.017 mol/L	First segment current density (A/m^2)	41.3	42.5	41.1
	Second segment current density (A/m^2)			51.5
	Third segment current density (A/m^2)		46.8	49
	Fourth segment current density (A/m^2)			57.3

Table C1
Applied voltage and measured current values for in dedicated tests for interference between electrodes segments assessment tests for Configuration 4.

Applied potential (V)	Current (A)	Current density (fictitious) (A/m^2)
0.1	0.025	1.23
0.2	0.047	2.35
0.3	0.066	3.30
0.4	0.082	4.08
0.5	0.095	4.73
0.6	0.108	5.35

Table C2
Applied voltage and measured current values for in dedicated tests for interference between electrodes segments assessment tests for Configuration 3.

Applied potential (V)	Current (A)	Current density (fictitious) (A/m^2)
0.1	0.020	0.5
0.2	0.039	0.98
0.3	0.059	1.48
0.4	0.075	1.88
0.5	0.088	2.20
0.6	0.100	2.50
0.7	0.111	2.78
0.8	0.122	3.05
0.9	0.132	3.30
1.0	0.141	3.53

tests with the total membrane area was therefore 4.1 W/m^2 ($\pm$0.2 W/m^2), at a high saline solution concentration of 5.0 mol/L, in Configuration 3 and at flow velocity of 2.0 cm/s. So, the electrode segmentation proved to be a significant feature to optimize energy harvesting in RED. However, care is needed to better exploit this feature. Indeed, in this experimental campaign, it was expected that the industrial scale RED unit would provide the best performance when operated in

Configuration 4, then in Configuration 3 and finally in Configuration 2.

On the other hand, several aspects should be considered.

First, tests with multiple electric circuits, Configurations 3 and 4, where conducted with the aim of maximizing the power density for each electrode segments pair separately, by varying local external resistances to seek the local maximum power. This methodology was adopted to investigate the possible use of adaptive external loads (e.g. Maximum Power Point Tracking), which could be applied to each circuit seeking for the maximum power output. An example of this research for the optimum condition is discussed in Section 2.4 in Supporting Information. However, it has been reported that the maximum power density for each segment do not necessary correspond to the overall maximum [38], since excessive consumption of salinity gradient in the initial sections of the stack may compromise power harvesting in the subsequent section. Moreover, it has been reported that one drawback of electrode segmentation is the possible mutual interactions among segments [58,59]. The adopted set-up was more sensible to such interactions due to the presence of a single ERS compartment, which indirectly connected the different electrode segments [60]. Therefore, the absence of stand-alone ERS compartments for each pair of segmented electrodes prevented complete electrical isolation. As a result, each time an electric circuit was connected to a pair of electrode segments, the electric current paths of adjacent segments could be influenced, leading to a significant power loss. This effect can impact the effectiveness of electrode segmentation feature. Detailed data for current and electromotive forces at each electrode segment are reported in Appendix B, and an assessment of the mutual interference between electrode segments is reported in Appendix C, which highlights how much the interference can be relevant (up to 25% of the useful current density values in the stack). This provides a clear indication of a route for performance improvement, by optimizing ERS compartments and reducing such dissipative phenomena.

The results obtained in this analysis can therefore be explained as follows: (i) Configuration 4 generally performed worse than Configuration 3, as the higher number of segments and, consequently, the greater number of connected loads amplified the influence of the previously discussed limiting factors on RED performance; (ii) the tests conducted with a high saline solution concentration of 1.0 mol/L, corresponding to the lowest salinity gradient investigated in this study, were the most affected by these limitations. In such conditions, electrode segmentation proved to be a suboptimal design choice, as the limited available power density, and the smaller variation in solution concentration observed along the channel, made these tests more sensitive to the aforementioned constraints.

Due to the poor performance of Configurations 3 and 4 at high saline solution C_H = 1.0 mol/L, as well as to the better performance of Configuration 3 compared to Configuration 4, it may be suggested the use of a modelling tool for a preliminary analysis of the best external loads arrangements in order to match external loads values that maximize the overall power output of the unit [38].

3.3. Comparison between upscaled RED stacks with and without electrode segmentation

In this section, RED stack performance of the present investigation is compared to literature studies on RED units with similar objectives, namely, electrode segmentation and upscaled units. Table 3 presents and compares the characteristics and performance of the stack used in this work with those reported by Veerman et al. [39] and Pintossi et al. [38].

The use of highly concentrated saline solutions in this study was the main parameter that led to an enhancement in power density, representing a clear step forward compared to previous works on electrode segmentation in RED units. Note that, the adopted here RED unit also exhibited the highest maximum power density increase due to segmentation among the studies.

Table 4 presents a review of studies employing upscaled RED units. Only RED stacks with channel lengths greater than 40 cm were considered.

Although the operating conditions and system configurations differ among the studies reviewed in Table 4, the present work exhibits superior power density performance, particularly under high-salinity conditions and elevated flow velocities. The maximum net power density achieved in this study, 4.1 W/m^2, exceeds the highest value reported for upscaled stacks in the literature.

4. Conclusions

In this work, the performance of a 10 × 80 cm^2 upscaled RED unit equipped with segmented electrodes was investigated via an extensive experimental campaign exploring several operating conditions and four electrode configurations. Tests conducted using a single electric circuit to assess the influence of channel length on RED performance confirmed that longer channels can boost power output and energy conversion in the RED process. Although the highest power density values were obtained in Configuration 1, with peak values of 6.7 W/m^2 (for C_H = 5.0 mol/L and 2.0 cm/s) and 6.1 W/m^2 (for C_H = 5.0 mol/L and 1.0 cm/s), for gross and net power density, respectively, the full utilization of the industrial scale channel length (Configuration 2) enabled a power output increase by at least a factor of two at the same operating conditions, as highlighted from the values of net energy efficiency, net power and yield. The values of yield reached in this worked marked a notable improvement with respect to previous literature studies.

In the analysis on electrode segmentation, Configuration 2 (i.e. one electric circuit), surprisingly performed better than Configuration 3 (i.e. two electric circuits) and Configuration 4 (i.e. four electric circuits) at the lowest high saline solution concentration (C_H = 1.0 mol/L). Configuration 4 exhibited worse performance than Configuration 3 almost in all cases, Configuration 3 provided the best result of 4.1 W/m^2 at the high saline solution concentration of 5.0 mol/L and solution velocity of 2.0 cm/s, with an increase of 21% with respect to Configuration 2, marking the advantages of using an electrode segmentation strategy in RED applications. The identification of Configuration 3 as best electrodes configuration is, however, biased by the limitations of the adopted unit (i.e. electrode segments interaction). On the other hand, some useful guidelines for the adoption of electrode segmentation can be provided: (i) the use of a modelling tool for a preliminary analysis of the best external resistances arrangement to be adopted and (ii) properly designed ERS compartments, which must isolate each electrode/ERS segment. These guidelines can be followed to overcome the aforementioned limitations and thoroughly assess the potential of electrode segmentation feature in RED unit.

The present work confirmed the use of electrode segmentation as a promising strategy for energy optimization in RED units, also for saline concentration up to 5.0 mol/L.

Moreover, the advantages of a RED unit with industrial scale length channels were highlighted and thoroughly assessed in this work, also providing practical recommendations for managing and properly operating upscaled set-ups and thus increasing the (TRL) of the RED process.

CRediT authorship contribution statement

Francesco Volpe: Conceptualization, Data curation, Formal analysis, Investigation, Methodology, Visualization, Writing – original draft. **Emanuela Mangiaracina:** Conceptualization, Data curation, Investigation, Methodology. **Giuseppe Battaglia:** Conceptualization, Data curation, Visualization, Writing – review & editing. **Andrea Cipollina:** Conceptualization, Funding acquisition, Project administration, Resources, Supervision, Writing – review & editing. **Giorgio Micale:** Conceptualization, Funding acquisition, Project administration, Resources, Supervision. **Alessandro Tamburini:** Conceptualization, Funding acquisition, Project administration, Resources, Supervision, Writing – review & editing.

Declaration of competing interest

The authors declare that they have no known competing financial interests or personal relationships that could have appeared to influence the work reported in this paper.

Acknowledgments

This project has received funding from the European Union's Horizon 2020 research and innovation programme under Grant Agreement No. 869467 (SEArcularMINE). This output reflects only the author's view. The European Health and Digital Executive Agency (HaDEA) and the European Commission cannot be held responsible for any use that may be made of the information contained therein. The authors are grateful to Deukum GmbH for their valuable advice, which was essential for carrying out the experimental procedures implemented in this work.

Appendix A. Effect of permselectivity and quantitative analysis of net power variation passing from Configuration 1 to Configuration 2

A.1. Effect of permselectivity on $P_{d,net}$ and theoretical $P_{d,net}$

The reduction in permselectivity due to the use of hypersaline solutions may hinder the performance of a RED unit. The most evident effect is observed in OCV values, as discussed in the main text. However, non-ideal permselectivity also contributes to potential losses in the generated power output. According to Eq. (4), a permselectivity of 90% already entails a reduction of approximately 20% in power output compared to the ideal case (i.e. membranes with 100% permselectivity). In this work, the estimated theoretical $P_{d,net}$ was calculated as follows: first permselectivity values were estimated for cases conducted at 2.0 cm/s for Configuration 1 at different high saline solution concentrations, then estimated permselectivity values were applied in Eq. (4) to determine the theoretical gross power density from experimental data that are intrinsically affected by non-ideal permselectivity and finally Eq. (5) was used to calculate the theoretical $P_{d,net}$ values (i.e., the power density achievable with ideal membranes). Table A1 reports the operating conditions of the experimental tests along with both experimental and theoretical $P_{d,net}$.

Regardless of the configuration, $P_{d,net}$ deviations from the ideal values varied consistently with permselectivity, with discrepancies being highest at $C_H = 5.0$ mol/L, followed by 2.5 mol/L and 1.0 mol/L. At $C_H = 1.0$ mol/L, the power density losses with respect to the theoretical value was 10%. For $C_H = 2.5$ mol/L, discrepancies with the theoretical $P_{d,net}$ reached 30–35%, with slightly higher values at a flow velocity of 2.0 cm/s. The largest discrepancies were observed at $C_H = 5.0$ mol/L, around 50%, and increased further with flow velocity.

A.2. Quantitative analysis of net power variation passing from Configuration 1 to Configuration 2

As discussed in the main text, RED units equipped with long channels exhibit, on average, a reduced salinity gradient due to more extensive salt passage along the flow path. However, although the OCV values are reduced, the increased salt passage through a large membrane area allowed higher conductivity of the low saline solution to attain along the channel thus reducing the stack resistance. Table A2 reports and compares OCV, stack resistance and net power for all the tests performed in Configuration 1 and 2.

It can be observed, on average, that OCV values reduced of about 20% when moving from Configuration 1 to Configuration 2, whereas the stack resistance decreased by a factor of ~3–4, thus leading to an overall enhancement of the power output (Eq. (4)).

The largest improvements in net power were achieved in tests adopting a $C_H = 5.0$ mol/L. This can be attributed to: (i) the largest variation in the low saline solution concentration, (ii) the smallest relative variation in the salt content of the high saline compartment, and (iii) the less attenuated OCV values along the channel length.

Appendix B. Current density and electromotive force distribution in segmented electrode configurations

With electrode segmentation, multiple external loads can be connected to a RED unit. This approach enables to account for the evolution of stack resistance and to independently optimize the external load for each section of the stack. Moreover, the electrode segmentation allows to monitor variations in current density and electromotive force along the channel length. Table B1 and B2 report OCV and current density values for tests performed in Configuration 2, 3 and 4.

OCV values decreased between segments as a result concentration gradient attenuation. OCV values between the first and the last segment reduced, see Configuration 4, by approximately 30–50% with the exception for the test carried out with a high saline solution concentration of 5.0 mol/L and a flow velocity of 0.5 cm/s, where the reduction exceeded 55%. Higher saline concentration and flow velocity enabled to preserve the salinity gradient along the channel. As expected, for each set of operating conditions, the highest OCV values were achieved at the first electrode segment.

A fairly homogeneous current density distribution was attained along the channel length with no significant drops near the outlet regions, e.g. in the fourth segment in Configuration 4. In Configuration 4, the current density initially increased along the channel (from the first to the second segment, and in most tests also from the second to the third). This behaviour is due to the decrease of local resistance along the channel length, which effect prevails on the electromotive force reduction. Therefore, lower current density values were observed at the first segments due to the lowest conductivity of the low saline solutions affecting local stack resistance. The increasing trend of current along the electrode segments was more pronounced at higher flow velocities (where electromotive force reduced less steeply) and at higher saline concentrations (where a significant salinity gradient was likely maintained even near outlet regions). On the average, regardless the configuration, current density increased with concentration and flow velocity.

Appendix C. Mutual interferences between electrode segments

As discussed in the main manuscript, mutual interferences between electrode segments were observed in tests performed in Configuration 3 and 4. This can be attributed to parasitic currents established by the potential difference between adjacent electrodes wet by the same ERS. To estimate the magnitude and relevance of potential parasitic currents, dedicated tests were carried out. Specifically, electrode segments of two adjacent circuits (i.e. the first segment to the second one for Configuration 4; the first two segments with the remaining two for Configuration 3) were connected through a

power supply (Elektro-Automatik EA-PS 2042-10B) and a voltage difference was applied, while only ERS flowed through its channel. Table C1 and C2 report the current values measured in the dedicated tests at applied potential values from 0.1 V to 1.0 V and a fictitious current density calculated dividing the measured current by the area of 1 electrode (10 × 20 cm^2) in Config. 4 and 2 electrodes (10 × 40 cm^2) in Config. 3, respectively. Applied voltage values were chosen in accordance with voltage differences between segments measured in experiments.

Measured current values were not negligible, thus confirming that electrode segments mutual interference had a significant impact on results reported in section 3.2 of the main text. As an example, considering the case of flow velocity of 0.5 cm/s, C_H = 1.0 mol/L, C_L = 0.017 mol/L, the measured difference in electromotive force between the first two segments is ~0.5 V (see the first two lines of Table B1) that can lead to a parasitic current of 0.0945 A (see Table C1) that corresponds to a current density of 4.73 A/m^2, which is 25% of the current density measured at the first electrode segment during the test, i.e. 18.8 A/m^2 (see Table B2).

Appendix D. Supplementary data

Supplementary data to this article can be found online at https://doi.org/10.1016/j.seppur.2025.135857.

Data availability

Data will be made available on request.

References

[1] D. Gielen, F. Boshell, D. Saygin, M.D. Bazilian, N. Wagner, R. Gorini, The role of renewable energy in the global energy transformation, Energy, Strateg. Rev. 24 (2019) 38–50, https://doi.org/10.1016/j.esr.2019.01.006.

[2] L. Li, J. Lin, N. Wu, S. Xie, C. Meng, Y. Zheng, X. Wang, Y. Zhao, Review and outlook on the international renewable energy development, Energy, Built Environ. 3 (2022) 139–157, https://doi.org/10.1016/j.enbenv.2020.12.002.

[3] M. Tedesco, A. Cipollina, A. Tamburini, G. Micale, Towards 1 kW power production in a reverse electrodialysis pilot plant with saline waters and concentrated brines, J. Membr. Sci. 522 (2017) 226–236, https://doi.org/10.1016/j.memsci.2016.09.015.

[4] J. Kuleszo, C. Kroeze, J. Post, B.M. Fekete, The potential of blue energy for reducing emissions of CO2 and non-CO2 greenhouse gases, J. Integr. Environ. Sci. 7 (2010) 89–96, https://doi.org/10.1080/19438151003680850.

[5] IEA, Electricity 2024: Analysis and forecast to 2026, IEA Publ. (2024) 1–170. https://www.iea.org/news/global-coal-demand-expected-to-decline-in-coming-years.

[6] W.J. Van Egmond, M. Saakes, S. Porada, T. Meuwissen, C.J.N. Buisman, H.V. M. Hamelers, The concentration gradient flow battery as electricity storage system: Technology potential and energy dissipation, J. Power Sources 325 (2016) 129–139, https://doi.org/10.1016/j.jpowsour.2016.05.130.

[7] A. Cipollina, G. Micale, Sustainable Energy from Salinity Gradients (2016), https://doi.org/10.1016/C2014-0-03709-4.

[8] H. Bie, L. Xue, Y. Wang, Z. Hao, G. Liu, Y. Li, Z. Lin, W. An, Effects of secondary impinging on flow features and mixing performance in T-T jet reactors, Chem. Eng. J. 454 (2023), https://doi.org/10.1016/j.cej.2022.140368.

[9] E.T. Expertise, EnTEC, n.d. doi:https://doi.org/10.2833/360619.

[10] R.E. Lacey, Energy by reverse electrodialysis, Ocean Eng. 7 (1980) 1–47, https://doi.org/10.1016/0029-8018(80)90030-X.

[11] D. Jin, Y. Cui, Y. Jin, Effect of spacer geometry on reverse electrodialysis stack performance, Desalination 602 (2025) 118652, https://doi.org/10.1016/j.desal.2025.118652.

[12] X. Wu, D. Sun, J. Lv, Y. Lv, S. Xu, X. Zhu, The spacer characteristic effect on hydrogen and electricity co-generation of a reverse electrodialysis stack driven by the salinity gradient of aqueous potassium acetate solutions, Energy 331 (2025), https://doi.org/10.1016/j.energy.2025.137041.

[13] S. Jomaa, S. Besbes, Parametric analysis of reverse electrodialysis process for improved power generation: Influence of spacer thickness, feed solution flow rate, membrane, and concentration, J Water Process Eng 66 (2024) 106024, https://doi.org/10.1016/j.jwpe.2024.106024.

[14] J.W. Post, C.H. Goeting, J. Valk, S. Goinga, J. Veerman, H.V.M. Hamelers, P.J.F. M. Hack, M. Turek, B. Bandura, Towards implementation of reverse electrodialysis for power generation from salinity gradients, Desalin. Water Treat. 205 (2010) 67–74, https://doi.org/10.1016/j.desal.2006.04.041.

[15] R.A. Tufa, S. Pawlowski, J. Veerman, K. Bouzek, E. Fontananova, G. di Profio, S. Velizarov, J. Goulão Crespo, K. Nijmeijer, E. Curcio, Progress and prospects in reverse electrodialysis for salinity gradient energy conversion and storage, Appl. Energy 225 (2018) 290–331, https://doi.org/10.1016/j.apenergy.2018.04.111.

[16] D.A. Vermaas, D. Kunteng, M. Saakes, K. Nijmeijer, Fouling in reverse electrodialysis under natural conditions, Water Res. 47 (2012) 1289–1298, https://doi.org/10.1016/j.watres.2012.11.053.

[17] A.H. Avci, R.A. Tufa, E. Fontananova, G. Di Profio, E. Curcio, Reverse Electrodialysis for energy production from natural river water and seawater, Energy 165 (2018) 512–521, https://doi.org/10.1016/j.energy.2018.09.111.

[18] M. Tedesco, A. Cipollina, A. Tamburini, G. Micale, J. Helsen, M. Papapetrou, REAPower: use of desalination brine for power production through reverse electrodialysis, Desalin. Water Treat. 53 (2015) 3161–3169, https://doi.org/10.1080/19443994.2014.934102.

[19] M. Mujahid, C. Wang, M. Umar Farooq, L. Feng, Y. Qiu, J. Li, H. Gao, L.F. Ren, J. Shao, Synergistic optimization of membrane distillation-reverse electrodialysis for sustainable desalination and salinity gradient power generation, Sep. Purif. Technol. 360 (2025) 130953, https://doi.org/10.1016/j.seppur.2024.130953.

[20] S. Santoro, R. Ashu, A. Halil, E. Fontananova, G. Di, E. Curcio, Fouling propensity in reverse electrodialysis operated with hypersaline brine 228 (2021), https://doi.org/10.1016/j.energy.2021.120563.

[21] R.A. Tufa, Y. Noviello, G. Di Profio, F. Macedonio, A. Ali, E. Drioli, E. Fontananova, K. Bouzek, E. Curcio, Integrated membrane distillation-reverse electrodialysis system for energy-efficient seawater desalination, Appl. Energy 253 (2019) 113551, https://doi.org/10.1016/j.apenergy.2019.113551.

[22] M. Yasukawa, S. Mehdizadeh, T. Sakurada, T. Abo, M. Kuno, M. Higa, Power generation performance of a bench-scale reverse electrodialysis stack using wastewater discharged from sewage treatment and seawater reverse osmosis, Desalination 491 (2020) 114449, https://doi.org/10.1016/j.desal.2020.114449.

[23] L. Gómez-Coma, V.M. Ortiz-Martínez, M. Fallanza, A. Ortiz, R. Ibañez, I. Ortiz, Blue energy for sustainable water reclamation in WWTPs, J Water Process Eng 33 (2020) 101020, https://doi.org/10.1016/j.jwpe.2019.101020.

[24] J.Y. Nam, K.S. Hwang, H.C. Kim, H. Jeong, H. Kim, E. Jwa, S.C. Yang, J. Choi, C. S. Kim, J.H. Han, N. Jeong, Assessing the behavior of the feed-water constituents of a pilot-scale 1000-cell-pair reverse electrodialysis with seawater and municipal wastewater effluent, Water Res. 148 (2019) 261–271, https://doi.org/10.1016/j.watres.2018.10.054.

[25] Q. Leng, F. Li, Y. Ma, L. Wang, S. Li, C. Zhang, Z. Wang, X. Wu, Direct oxidation of wastewater degradation and hydrogen production simultaneously by a reverse electrodialysis system powered by salinity gradient energy, J. Environ. Chem. Eng. 13 (2025), https://doi.org/10.1016/j.jece.2025.116461.

[26] Z. Seifollahi, M. Khatibi, S.N. Ashrafizadeh, Ionic Transport Behavior of Soft Nanochannels for Newtonian and Non-Newtonian Electrolytes, Ind. Eng. Chem. Res. 63 (2024) 10812–10824, https://doi.org/10.1021/acs.iecr.4c01176.

[27] S. Jafari, M. Khatibi, S.N. Ashrafizadeh, Blue energy conversion utilizing smart ionic nanotransistors, Electrochim. Acta 507 (2024) 145186, https://doi.org/10.1016/j.electacta.2024.145186.

[28] H. Dartoomi, M. Khatibi, S.N. Ashrafizadeh, Enhanced Ionic Current Rectification through Innovative Integration of Polyelectrolyte Bilayers and Charged-Wall Smart Nanochannels, Anal. Chem. 95 (2023) 1522–1531, https://doi.org/10.1021/acs.analchem.2c04559.

[29] A. Aminnia, M. Khatibi, S. Nezameddin Ashrafizadeh, Fouling minimization with nanofluidic membranes; How electric field may help, Sep. Purif. Technol. 325 (2023) 124698, https://doi.org/10.1016/j.seppur.2023.124698.

[30] M. Khatibi, S.N. Ashrafizadeh, Ion Transport in Intelligent Nanochannels: A Comparative Analysis of the Role of Electric Field, Anal. Chem. 95 (2023) 18188–18198, https://doi.org/10.1021/acs.analchem.3c03809.

[31] M. Khatibi, H. Dartoomi, S.N. Ashrafizadeh, Layer-by-Layer Nanofluidic Membranes for Promoting Blue Energy Conversion, Langmuir 39 (2023) 13717–13734, https://doi.org/10.1021/acs.langmuir.3c01962.

[32] X. Wu, X. Zhang, S. Xu, Y. Gong, S. Yang, D. Jin, Performance of a reverse electrodialysis cell working with potassium acetate−methanol−water solution, Energy 232 (2021), https://doi.org/10.1016/j.energy.2021.120944.

[33] E. Altiok, T.Z. Kaya, K. Smolinska-Kempisty, E. Güler, N. Kabay, B. Tomaszewska, M. Bryjak, Salinity gradient energy conversion by custom-made interpolymer ion exchange membranes utilized in reverse electrodialysis system, J. Environ. Chem. Eng. 11 (2023), https://doi.org/10.1016/j.jece.2023.109386.

[34] A. Siekierka, F. Yalcinkaya, M. Bryjak, Recovery of transition metal ions with simultaneous power generation by reverse electrodialysis, J. Environ. Chem. Eng. 11 (2023) 110145, https://doi.org/10.1016/j.jece.2023.110145.

[35] H. Kang, B. Koo, H. Chai, S.P. Jung, Impedance characteristics and polarization behaviors of microbial reverse-electrodialysis cells with changes in effective membrane area, intermembrane distance, and flow rates of salinity gradient waters, J. Environ. Chem. Eng. 12 (2024) 114313, https://doi.org/10.1016/j.jece.2024.114313.

[36] S. Bevinakatti, J. Hwan Kim, J. Woo Park, Optimized sustainable development for phosphorus separation with electricity generation in a novel aluminum-air reverse electrodialysis, Sep. Purif. Technol. 355 (2025) 129576, https://doi.org/10.1016/j.seppur.2024.129576.

[37] A. Daniilidis, R. Herber, D.A. Vermaas, Upscale potential and financial feasibility of a reverse electrodialysis power plant, Appl. Energy 119 (2014) 257–265, https://doi.org/10.1016/j.apenergy.2013.12.066.

[38] C. Simões, D. Pintossi, M. Saakes, Z. Borneman, W. Brilman, Electrode segmentation in reverse electrodialysis : Improved power and energy efficiency, Desalination 492 (2020) 114604, https://doi.org/10.1016/j.desal.2020.114604.
[39] S.J. Veerman, Saakes Joost, Metz Michel, G.J.A.N. Harmsen, Electrical power from sea and river water by reverse electrodialysis: A first step from the laboratory to a real power plant 44 (2010) 9207–9212.
[40] M. Kim, S. Kim, J. Choi, H. Kim, N. Jeong, R. Kwak, Numerical analysis of real-scale reverse electrodialysis with microscale structures and electrode segmentation, Chem. Eng. J. 446 (2022) 1–29, https://doi.org/10.1016/j.cej.2022.137357.
[41] J. Veerman, M. Saakes, S.J. Metz, G.J. Harmsen, Reverse electrodialysis: A validated process model for design and optimization, Chem. Eng. J. 166 (2011) 256–268, https://doi.org/10.1016/j.cej.2010.10.071.
[42] A. Filingeri, L. Gurreri, M. Ciofalo, A. Cipollina, A. Tamburini, G. Micale, Current distribution along electrodialysis stacks and its influence on the current-voltage curve: behaviour from near-zero current to limiting plateau, Desalination 556 (2023) 116541, https://doi.org/10.1016/j.desal.2023.116541.
[43] J. Moreno, S. Grasman, R. Van Engelen, K. Nijmeijer, Upscaling Reverse Electrodialysis, Environ. Sci. Technol. 52 (2018) 10856–10863, https://doi.org/10.1021/acs.est.8b01886.
[44] M. Tedesco, C. Scalici, D. Vaccari, A. Cipollina, A. Tamburini, G. Micale, Performance of the first reverse electrodialysis pilot plant for power production from saline waters and concentrated brines, J. Membr. Sci. 500 (2016) 33–45, https://doi.org/10.1016/j.memsci.2015.10.057.
[45] J. Luque, D. Salvo, A. Cosenza, A. Tamburini, G. Micale, A. Cipollina, Long-run operation of a reverse electrodialysis system fed with wastewaters, J. Environ. Manag. 217 (2018) 871–887, https://doi.org/10.1016/j.jenvman.2018.03.110.
[46] A. Cosenza, G. Campisi, F. Giacalone, S. Randazzo, A. Cipollina, A. Tamburini, G. Micale, Power Production from Produced Waters via Reverse Electrodialysis: A Preliminary Assessment, Energies 15 (2022), https://doi.org/10.3390/en15114177.
[47] D.A. Vermaas, D. Kunteng, J. Veerman, M. Saakes, K. Nijmeijer, Periodic feedwater reversal and air sparging as antifouling strategies in reverse electrodialysis, (2014).
[48] D.A. Vermaas, M. Saakes, K. Nijmeijer, Early detection of preferential channeling in reverse electrodialysis, Electrochim. Acta 117 (2014) 9–17, https://doi.org/10.1016/j.electacta.2013.11.094.
[49] L. Gurreri, A. Tamburini, A. Cipollina, G. Micale, M. Ciofalo, CFD prediction of concentration polarization phenomena in spacer- fi lled channels for reverse electrodialysis, J. Membr. Sci. 468 (2014) 133–148, https://doi.org/10.1016/j.memsci.2014.05.058.
[50] M. Tedesco, E. Brauns, A. Cipollina, G. Micale, P. Modica, G. Russo, J. Helsen, Reverse electrodialysis with saline waters and concentrated brines: A laboratory investigation towards technology scale-up, J. Membr. Sci. 492 (2015) 9–20, https://doi.org/10.1016/j.memsci.2015.05.020.
[51] J.L. Di Salvo, A. Cosenza, A. Cipollina, A. Tamburinia, G. Micale, Experimental analysis of a continuously operated reverse electrodialysis unit fed with wastewaters, Chem. Eng. Trans. 60 (2017) 307–312, https://doi.org/10.3303/CET1760052.
[52] M. Micari, M. Bevacqua, A. Cipollina, A. Tamburini, W. Van Baak, T. Putts, G. Micale, Effect of different aqueous solutions of pure salts and salt mixtures in reverse electrodialysis systems for closed-loop applications, J. Membr. Sci. 551 (2018) 315–325, https://doi.org/10.1016/j.memsci.2018.01.036.
[53] M. Bevacqua, A. Tamburini, M. Papapetrou, A. Cipollina, G. Micale, A. Piacentino, Reverse electrodialysis with NH4HCO3-water systems for heat-to-power conversion, Energy 137 (2017) 1293–1307, https://doi.org/10.1016/j.energy.2017.07.012.
[54] S. Pawlowski, J.G. Crespo, S. Velizarov, Pressure drop in reverse electrodialysis: Experimental and modeling studies for stacks with variable number of cell pairs, J. Membr. Sci. 462 (2014) 96–111, https://doi.org/10.1016/j.memsci.2014.03.020.
[55] K.W. Krakhella, M. Morales, R. Bock, F. Seland, O.S. Burheim, K.E. Einarsrud, Electrodialytic energy storage system: Permselectivity, stack measurements and life-cycle analysis, Energies 13 (2020) 1–26, https://doi.org/10.3390/en13051247.
[56] A. Daniilidis, D.A. Vermaas, R. Herber, K. Nijmeijer, Experimentally obtainable energy from mixing river water, seawater or brines with reverse electrodialysis, Renew. Energy 64 (2014) 123–131, https://doi.org/10.1016/j.renene.2013.11.001.
[57] F. Giacalone, M. Papapetrou, G. Kosmadakis, A. Tamburini, G. Micale, A. Cipollina, Application of reverse electrodialysis to site-specific types of saline solutions: A techno-economic assessment, Energy 181 (2019) 532–547, https://doi.org/10.1016/j.energy.2019.05.161.
[58] J. Veerman, Reverse electrodialysis: Co-and counterflow optimization of multistage configurations for maximum energy efficiency, Membranes (Basel). 10 (2020) 1–13, https://doi.org/10.3390/membranes10090206.
[59] D. Tvrzník, Effect of electrode area on demineralization performance and the distribution of current density in an industrial-scale electrodialysis stack, Desalination 412 (2017) 49–57, https://doi.org/10.1016/j.desal.2017.03.002.
[60] G. Doornbusch, H. Swart, M. Tedesco, J. Post, Z. Borneman, K. Nijmeijer, Current utilization in electrodialysis: Electrode segmentation as alternative for multistaging, Desalination 480 (2020) 114243, https://doi.org/10.1016/j.desal.2019.114243.